Research Square

Preprints are preliminary reports that have not undergone peer review.
They should not be considered conclusive, used to inform clinical practice,
or referenced by the media as validated information.

Attosecond dynamics of photoemission over a wide photon energy range

Christian Schröder (christian.schroeder@tum.de)
TUM School of Natural Sciences

Johann Riemensberger
Swiss federal Institute of Technology Lausanne (EPFL) https://orcid.org/0000-0002-3468-6501

Roman Kuzian
Donostia International Physics Center (DIPC) https://orcid.org/0000-0002-6672-7224

Marcus Ossiander
Technical University Munich

Dyonisios Potamianos
Max Planck Institute of Quantum Optics

Francesco Allegrett
Physics Department E20, Technical University of Munich

Luca Bignardi
University of Trieste https://orcid.org/0000-0002-9846-9100

Silvano Lizzit
Elettra - Sincrotrone Trieste S.C.p.A.

Ayman Akil
Max Planck Institute of Quantum Optics https://orcid.org/0000-0003-0104-5369

Adrian Cavalieri
Paul Scherrer Institute

Dietrich Menzel
TUM School of Natural Sciences https://orcid.org/0000-0002-7188-8532

Stefan Neppl
Paul Scherrer Institute

Raph Ernstorfer
Fritz Haber Institute

Jürgen Braun
Ludwig-Maximilians-Universität München

Hubert Ebert
Ludwig-Maximilians-Universität München

Jan Minar
University of West Bohemia https://orcid.org/0000-0001-9735-8479

Wolfram Helml

Technische Universität Dortmund https://orcid.org/0000-0003-1537-2993
Michael Jobst
TUM School of Natural Sciences
Michael Gerl
TUM School of Natural Sciences
Elisabeth Bothschafter
TUM School of Natural Sciences
Andreas Kim
TUM School of Natural Sciences
Konrad Hütten
TUM School of Natural Sciences
Ulf Kleineberg
Max-Planck-Institut für Quantenoptik
Maximilian Schnitzenbaumer
Technical University of Munich
Johannes Barth
Technical University of Munich
Peter Feulner
TUM School of Natural Sciences
Eugene Krasovskii
Universidad del Pais Vasco https://orcid.org/0000-0003-4246-2986
Reinhard Kienberger
Technical University Munich https://orcid.org/0000-0001-8781-3685

Article

Keywords:

Posted Date: October 31st, 2023

DOI: https://doi.org/10.21203/rs.3.rs-3024896/v1

License: This work is licensed under a Creative Commons Attribution 4.0 International License.
Read Full License

Additional Declarations: There is **NO** Competing Interest.

Attosecond dynamics of photoemission over a wide photon energy range

Christian A. Schröder[1,*,†], Johann Riemensberger[1,*], Roman Kuzian[2,3], Marcus Ossiander[4,5], Dyonisios Potamianos[6], Francesco Allegretti[1], Luca Bignardi[7], Silvano Lizzit[8], Ayman Akil[6], Adrian Cavalieri[9,10], Dietrich Menzel[1], Stefan Neppl[10], Raph Ernstorfer[11,12], Jürgen Braun[13], Hubert Ebert[13], Jan Minar[14], Wolfram Helml[15], Michael Jobst[1], Michael Gerl[1], Elisabeth Bothschafter[1], Andreas Kim[1], Konrad Hütten[1], Ulf Kleineberg[6,16], Maximilian Schnitzenbaumer[1], Johannes Barth[1], Peter Feulner[1], Eugene Krasovskii[17,18,2], Reinhard Kienberger[1,†],

[1]Physics Department, TUM School of Natural Sciences, Garching, Germany

[2]Donostia International Physics Center (DIPC), San Sebastián/Donostia, Spain

[3]Frantsevich Institute for Problems of Materials Science NASU, Kiev, Ukraine

[4]Institute of Experimental Physics, Graz University of Technology, Graz, Austria

[5]John A. Paulson School of Engineering and Applied Sciences; Harvard University, Cambridge, USA

[6]Max Planck Institute of Quantum Optics, Garching, Germany

[7]Department of Physics, University of Trieste, Trieste, Italy

[8]Elettra - Sincrotrone Trieste S.C.p.A., Trieste, Italy

[9]Institute of Applied Physics, University of Bern, Bern, Switzerland

[10]Paul Scherrer Institute, Villigen, Switzerland

[11]Institute for Optics and Atomic Physics (IOAP), Technical University Berlin, Berlin Germany

[12]Department of Physical Chemistry, Fritz Haber Institute, Berlin, Germany

[13]Department Chemie, Ludwig-Maximilians-Universität München, München, Germany

[14]New Technologies-Research Center, University of West Bohemia, Pilsen, (Czech Republic)

[15]Zentrum für Synchrotronstrahlung, Fakultät Physik – Beschleunigerphysik, Technische Universität Dortmund, Dortmund, Germany

[16]Ludwig-Maximilians-Universität München (LMU), Garching, Germany.

[17]Departamento de Polímeros y Materiales Avanzados: Física, Química y Tecnología, Universidad del Pais Vasco UPV/EHU,San Sebastián/Donostia, Spain

[18]IKERBASQUE, Basque Foundation for Science, Bilbao, Spain

[†]To whom correspondence should be addressed:
E-mails: christian.schroeder@tum.de, reinhard.kienberger@tum.de

[*]These authors contributed equally.

Abstract

Dynamics of photoemission from surfaces are usually studied at low photon energies ($< 100\,\mathrm{eV}$). Here, we report on new findings on these dynamics observed at a tungsten surface on the attosecond time scale at photon energies exceeding 100 eV, over a range of almost 50 eV. While photoemission, a fundamental process in quantum mechanics, is often described within a semiclassical three-step model, we find that even at high photon energies only a full quantum treatment in one step predicts the measured attosecond dynamics correctly. On this time scale the intuitive, mechanistic interpretation of the photoelectric effect breaks down. This underlines the necessity to further develop experimental and theoretical tools to be used in improving our understanding of the fundamental process of light-matter interaction underlying many methods in extreme ultraviolet and soft x-ray spectroscopy.

Photoelectron spectroscopy is an important technique for the investigation of electronic properties of atoms, molecules and solid-state systems. Especially in the case of solids the energy- and angular distributions, and if available the spin of the photoelectrons liberated by light with a photon energy in excess of the binding energies of states of the system under study carries a plethora of information on its chemical composition [1], occupied electronic states and many-body correlations [2, 3]. With its extension towards attosecond temporal resolution via the attosecond streak camera technique (cf. e.g. [4, 5, 6]) or RABBITT (Reconstruction of Attosecond Beating by Interference of Two–photon Transitions) (cf. e.g. [7, 8, 9]), it became possible to time the underlying photoemission process itself whereby new fundamental questions concerning the nature and composition of the observed photoemission times arose. In this context, the tungsten (110) surface assumes a special position as the first system on which such a measurement has ever been performed [4] and furthermore it is the first solid–state system on which an absolute photoemission time, i.e., the time between the arrival of the extreme ultraviolet (XUV) photon at the solid–vacuum interface and the appearance of the electron in vacuum, has ever been determined experimentally [10].

Photoemission times can today be calculated to sub-attosecond precision for single atoms [11, 10], and recent progress has brought comparable accuracy to calculations on some molecular systems [12] facilitating accurate comparison of experiments and theoretical models for the dynamic photoemission process. The photoemission time delay can often be interpreted as the Eisenbud-Wigner-Smith delay time

$$\tau_{\mathrm{EWS}} = \frac{\partial}{\partial E} \arg\left\{d_{i\to f}(E)\right\}, \tag{1}$$

which relates to the energy derivative of the phase shift of the optical excitation matrix element

$$d_{i\to f}(E) = \langle \Psi_f | \mathbf{A}\cdot\mathbf{p} + \mathbf{p}\cdot\mathbf{A} | \Psi_i \rangle, \tag{2}$$

between the initial and final states Ψ_i and Ψ_f associated with the photoionization event (cf. [13], atomic units are used throughout unless indicated otherwise). In Eq. 2 $\mathbf{p}$ is the momentum operator and $\mathbf{A}$ is the vector potential of the light irradiating the sample.

For solid-state photoemission, a fully time-dependent simulation of the attosecond photoemission process remains out of reach. Hence, different interpretations have been brought forward based, e.g., on the role of surface- and bulk contributions and the escape depth of the photoelectrons [10, 7, 14], as well as the semiclassical electron transport in the solid with the group velocity $v_g(\mathbf{k})$ determined by the material's band structure [7, 15, 16, 17] which follows the initial excitation and has enjoyed considerable popularity even in the interpretation of time-integral photoemission experiments. A recently developed one-step theory of the photoelectron escape time [18] and its application to photoemission from a Mg(0001) surface demonstrated that the Eisenbud-Wigner-Smith formalism can be applied to semi-infinite crystals through the phase of the optical transition matrix element between the initial state and the final state of one-step photoemission theory, the so-called time-reversed low–energy electron diffraction (LEED) state. This way a clear interpretation of the photoemission times in terms of scattering arises within the well established quantum theory of stationary photoemission, without the need to artificially dissect the photoemission process into sequential steps. Here, we report on the application and validation of this theory by comparing its predictions to photoemission times measured on a W(110) surface for photon energies between 100 eV and 150 eV via attosecond streaking. We find – in contrast to semiclassical modelling – that the predicted relative photoelectron escape times agree well with the relative time delays of photoemission measured in the experiment over a large energy range of almost 50 eV.

Using a spectrogram inversion algorithm, we are furthermore able to infer upon the photoionization dynamics in an interval around the central photon energies studied, facilitating a broadband and piecewise continuous comparison of measured and calculated photoemission time delays. This underlines the important role of attosecond streaking spectroscopy as a powerful technique for the assessment of photoemission dynamics above $\sim 100\,\mathrm{eV}$.

Experiment

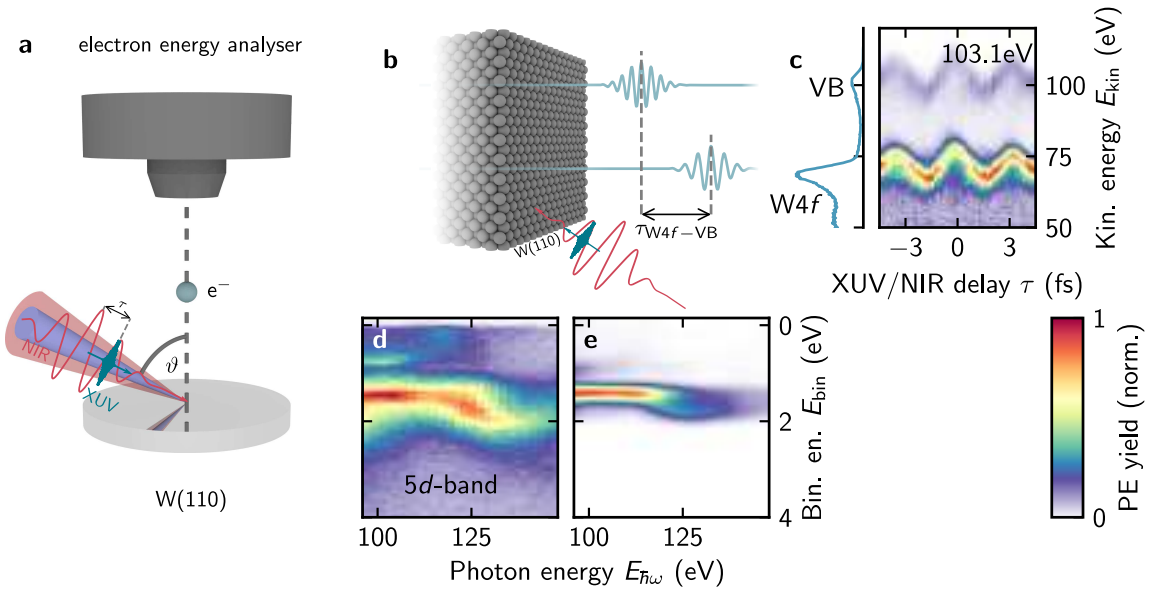

Figure 1: **Overview of the experiment. a** Geometry of the attosecond streaking experiment. The collinear XUV and NIR beams impinge onto the sample under an angle $\vartheta = 70°$ with respect to the surface normal. Photoelectrons are detected in a cone with opening angle either $\Delta = \pm 22°$ or $\Delta = \pm 2°$ around the surface normal with a time-of-flight (TOF) electron energy analyser. **b** Principle of solid state photoemission chronoscopy. Photoelectron wave packets liberated by the attosecond XUV pulse is a superposition of many plane-wave like components emanating from the solid upon photoexcitation. The variation of their relative phases with the kinetic energy gives rise to the observable photoemission delay. The NIR pulse maps this temporal information onto the spectral domain. **c** Exemplary streaking spectrogram recorded at a photon energy of 103.1 eV. **d** Angle-integrated high resolution photoelectron spectrogram of the W(110) valence band between 96 eV and 150 eV.**e** Calculated photoelectron spectrogram for normal emission. The replication of the general shape of the experimental spectrogram, especially the peculiar spoon-like feature at $\sim 130\,\mathrm{eV}$ demonstrates the accuracy of our calculations.

Figure 1a illustrates our experimental geometry. The experimental apparatus has been described elsewhere [19]. In summary, isolated p-polarized XUV pulses of a few hundred attoseconds in duration impinge onto a W(110) surface at an angle of $\vartheta = 70°$ and eject electrons from both the W4f core-levels and the valence band (VB). These evolve as wave packets inside the crystal, and are scattered by the crystal lattice. Upon exiting the crystal they undergo the action of a waveform-controlled near-infrared (NIR) laser pulse (pulse duration $\tau_{\mathrm{FWHM}} \approx 5\,\mathrm{fs}$, $\lambda_c = 780\,\mathrm{nm}$) propagating collinearly with the XUV pulse, resulting in a modulation of their final kinetic energy. The XUV penetrates deeply into the solid while the NIR pulse's action is strongly suppressed below the surface [20]. The action of the laser pulse maps the temporal information encoded in the photoelectron wave packet onto their energy spectra, which are recorded as a function of the delay between the XUV and the NIR pulse [21, 22] (Fig. 1b, c). Photoelectrons are detected with a time-of-flight (TOF) spectrometer with an acceptance angle set to $\Delta = \pm 22°$, corresponding to an integration over more than the first Brillouin zone. A set of such spectra combines into a spectrogram as exemplarily shown in Fig. 1c where the NIR-induced kinetic energy modulations are clearly visible. Negative values of the XUV/NIR delay

indicate that the NIR pulse arrives at the sample first. The attosecond XUV pulses are generated via high harmonic generation and extracted from the high-harmonic cut-off via spectral filtering using thin Zr and Pd metal foils and customized multilayer XUV reflectors (cf. e.g. [23]). XUV pulses centered at 103.1 eV, 110.1 eV, 117.1 eV, 124.4 eV, 133.7 eV and 145.0 eV with FWHM bandwidths of 4.6 eV, 3.5 eV, 4.0 eV, 4.8 eV, 4.0 eV and 3.5 eV were generated for the experiments (cf. Methods). In addition to the time-resolved measurements, high-resolution steady-state photoelectron spectra have been recorded at the SuperESCA beamline of the ELETTRA storage ring [24] (Fig. 1d) which were used for accurately determining the final-state band structure in the calculations. Comparison with Fig. 1e, which shows a calculated photoelectron spectrogram demonstrates the quality of our calculations. The replication of essential features of the high-resolution spectra, especially the spoon-shaped feature at $\sim$ 130 eV photon energy indicates that both initial and final state band structure are described well. The static valence band photoemission is strongly dominated by the W5*d*-band in our photon energy range. A band with *sp*-character is found at larger binding energies (see Extended Data), but it does not contribute significantly to the photoelectron signal in our region of interest. Our discussions pertaining the VB photoemission therefore refer solely to the 5*d* band unless noted otherwise.

Results

We study the relative escape time $\tau_{4f-\mathrm{VB}}$ between photoelectrons originating from the W4*f* states and those ejected from the valence band, which is encoded in the attosecond streaking spectrograms. At the energetic center of the streaking feature we extract $\tau_{\mathrm{W}4f-\mathrm{VB}}$ with a method based on fit to a restricted parametrization of the solution to the time-dependent Schrödinger equation for the attosecond streaking process (rTDSE for short, see Methods) [5, 25], with the results listed in Table 1.

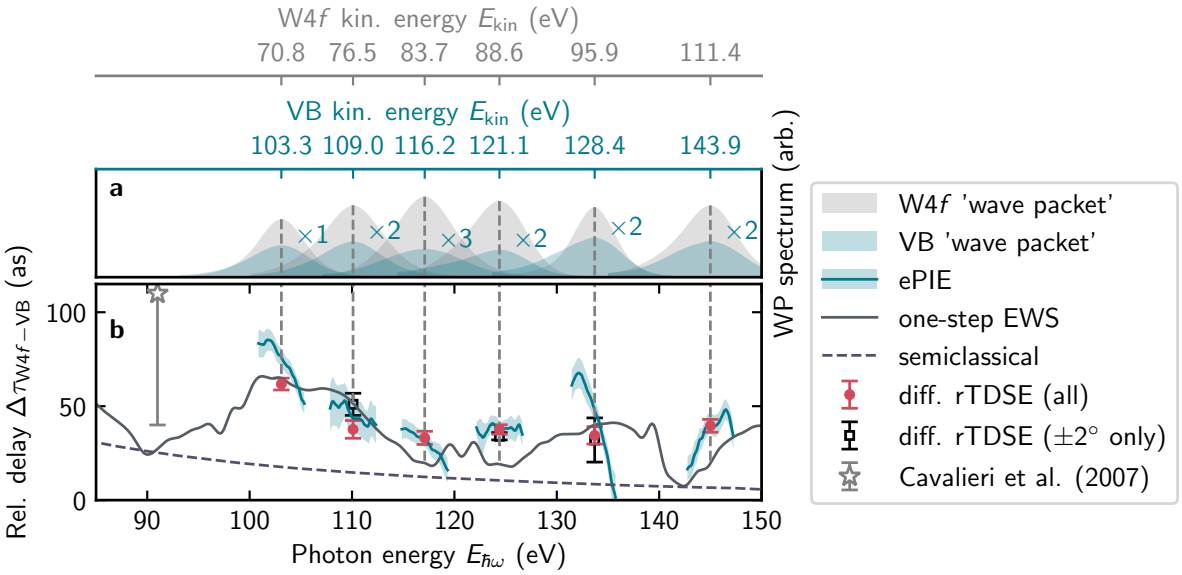

Figure 2: **Relative photoemission time delays.** Reconstructed "wave packet" spectra (**a**) and relative W4*f*-VB photoelectron escape times $\tau_{\mathrm{W}4f-\mathrm{VB}}$ (**b**), with the central kinetic energies of the 4*f* and VB photoemission denoted as separate axes on the top. The relative W4*f*-VB delay derived from the one-step calculation is plotted as a solid gray line. Red data points indicate the results of the rTDSE analysis and are generally in good agreement with the calculation, black squares show the rTDSE results for measurements taken with a small acceptance angle. Only at 110.1 eV we find a slight deviation. In the original experiment by Cavalieri et al. [4] (gray star) a relative photoemission time in excess of 100 as was measured at $\sim$ 91 eV, but due to its large uncertainty it cannot be readily compared to the calculation. The ePIE results are shown as solid blue lines with shaded areas indicating their uncertainty. Outside of where the reconstructed W4*f* and VB spectra have appreciable values no delay can be reported. The semiclassical relative escape time is shown as a dashed line. Its smooth shape cannot account for the strong modulations observed in the relative photoemission times.

In general, the measured spectrogram is an incoherent average of each possible transition between an initial state Ψ_i and the time-reversed LEED state Ψ_f mediated by the broadband XUV pulse, streaked by the few-cycle NIR pulse. Therefore, for comparison with the experiment, the individual calculated escape times $\tau_{i\to f} = \partial \arg\{d_{i\to f}(E)\}/\partial E$ for every such transition are also averaged. We find the relative $\tau_{\mathrm{W}4f-\mathrm{VB}}$ delays calculated this way for electron emission along the surface normal and the delays extracted from the experimental data with the rTDSE method to agree well (see Fig. 2). In order to test whether the integration over the Brillouin zone in the experiment changes the observed delay we performed a small subset of the measurements with an acceptance angle of $\Delta = \pm 2°$ at 110.1 eV, 124.4 eV and 133.7 eV. These are shown as black squares in Fig. 2 (see Methods). Only at 110.1 eV we find a difference between the mean of all delay values extracted at this energy and the subset of spectrograms recorded with the small acceptance angle. That the central photoemission time delays determined via attosecond streaking are quite insensitive to angular averaging has been observed before [14]. As the deviations are expected to be small and the signal-to-noise ratio is drastically enhanced the remaining measurements were taken with the large acceptance angle.

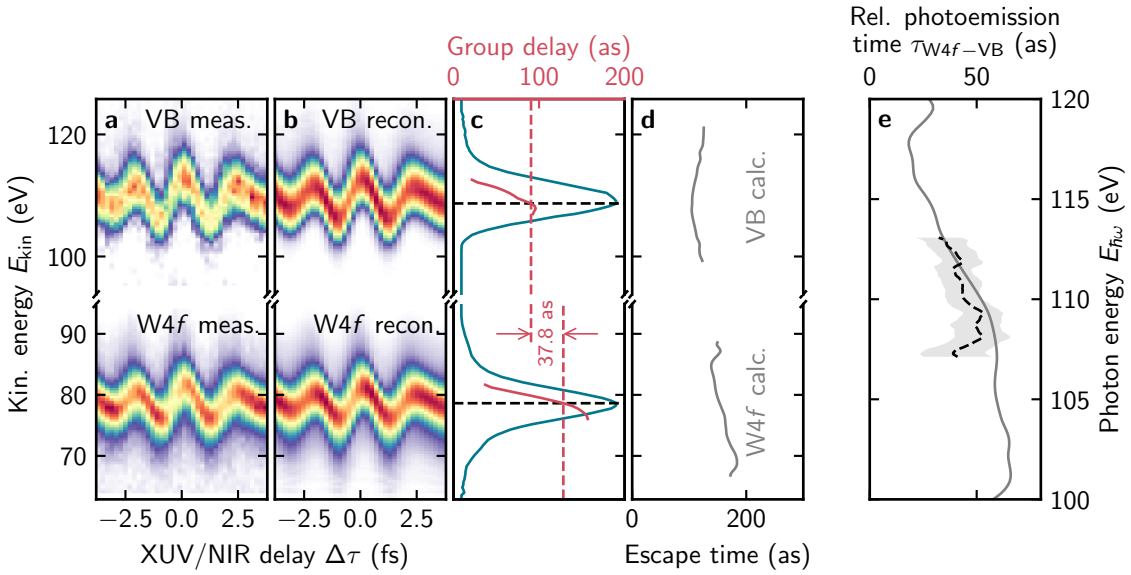

Figure 3: **Wave packet reconstruction.** Ptychographic spectrogram inversion for the inference of the energy dependent relative photoelectron escape time at 110.1 eV. An exemplary streaking spectrogram and its reconstruction are shown in panels **a** and **b**. Electron spectra (blue) and group delays (red) of the reconstructed effective "wave packets" (red lines, panel **c**). The sought-after timing information is encoded in their difference, in which the XUV pulse's chirp is canceled out. The W4f and VB escape times calculated in the EWS formalism around this photon energy are shown in panel **d**. In order to extract reliable relative escape times, we take the mean over many reconstructions (dashed black line in **e**). This also provides a measure of uncertainty (95% confidence interval, shaded gray area in **e**). The color map for the false-color plots can be found in Fig. 1.

While the rTDSE method extracts the delay information at the energetic center of the streaking features, the large XUV bandwidth suggests though that more information about the energy dependence of the photoemission dynamics could be extracted from a spectrogram. Attosecond streaking encodes spectral and temporal information on the outgoing photoelectron wave packet. For photoemission from a narrow atomic level (e.g. in a gas-phase experiment on a noble gas) a connection between the photoelectron spectrogram and the optical transition matrix element $d_{i\to f}(E)$ can be established [22]. The spectrogram is sensitive to the energy dependence of the photoelectron wave packet's phase and consequently its timing, and the complex amplitude and spectral phase of the wave packet can be reconstructed with the use of phase-retrieval algorithms [26, 27, 28]. The application of such an algorithm to a streaking spectrogram comprised of an incoherent average of different emission features (as it is the case here) cannot access $d_{i\to f}(E)$ directly, but time-energy information on the photoemission process is still recoverable (cf. [10]). Our retrieval algorithm is based on the extended ptychographic iterative engine (ePIE) [29], which is configured to retrieve two "wave packets", one

for the valence band and one for the W4f core–levels respectively from each spectrogram, under the constraint of both being streaked by the same NIR pulse (see Methods). The retrieved "wave packets" will share a common phase distortion due to the properties of the XUV pulse, which can be eliminated by subtracting their respective group delays after aligning their energetic centers. This procedure is illustrated in Fig. 3. The sharp and narrow features comprising the W4f and the VB photoemission are unresolved due to the large bandwidth of the XUV pulses. Within the regions where the VB and W4f photoelectron signal is appreciable ($\sim \pm 2.5\,\mathrm{eV}$ from the energetic center of the photoemission feature) one can expect the photon energy dependence of the escape time to become accessible. The relative escape times at the energetic center of the retrieved "wave packets" are summarized in Table 1, which are in good agreement with the results obtained with the rTDSE method. The energy dependence of the relative escape times is plotted in Fig. 2b as blue lines, with shaded blue areas indicating the 95% confidence interval. The general trend of the experimental delays is in accordance with the prediction of our one-step theory, however, distinct deviations in the slope occur at 103.1 eV and at 133.7 eV. The retrieved "wave packet" spectra for the W4f and VB photoemission are shown in Fig. 2a.

Table 1: Relative photoemission time delays determined at the energy centers of the reconstructed electron "wave packets". We find that both methods generally agree within their respective uncertainties (95% confidence interval).

$E_{\hbar\omega}$ [eV]	103.1	110.1	117.1
rTDSE [as]	(61.8 ± 3.2)	(37.6 ± 4.7)	(33.1 ± 3.5)
ePIE [as]	(76.2 ± 4.6)	(43.6 ± 8.4)	(33.2 ± 4.4)

$E_{\hbar\omega}$ [eV]	124.4	133.7	145.0
rTDSE [as]	(37.6 ± 2.5)	(34.5 ± 4.6)	(39.6 ± 3.4)
ePIE [as]	(35.9 ± 6.4)	(47.8 ± 6.8)	(41.4 ± 5.7)

Discussion

Photoemission time delays measured on metal surfaces have been interpreted in various ways, either resorting to one-dimensional models (cf. e.g. [30, 31, 14]) or to semiclassical considerations (cf. e.g. [4, 17, 15]) in the spirit of the three-step model of photoemission [32]. The three-step model treats the initial photoexcitation, the subsequent propagation of the photoelectron wave packet and finally its passage of the surface and detection as separate steps. The semiclassical arguments pertaining the transport step lead to the photoelectron escape time $\tau = (2V_i)^{-1}$ behaving inversely proportional to the optical potential V_i which is responsible for damping the outgoing wave inside the crystal [33]. The semiclassical model is expected to be an adequate prediction of the photoemission delay time far from band gaps in the final state spectrum and when lattice scattering of the photoelectron wavepacket is weak [33]. Here we probe a region where this semiclassical approach is not applicable and contrast this model with a full one-step treatment in three dimensions [18]. Inspecting the final state band structure of W(110) for normal emission reveals that the dominating conducting branch splits into an "upper branch" and a "lower branch" around a final state energy of 100 eV (Fig. 4b). At 103.1 eV photon energy the final states for VB electrons will coincide with this gap-like feature, and for 133.7 eV the W4f photoelectrons will coincide with the same gap (see Fig. 4b). In both cases, we find large positive excursions of the observed relative delay from the slowly decreasing relative escape time predicted semiclassically (see Fig. 2). With increasing final state energy, the fraction of the photocurrent carried by the "upper branch" decreases, while that of the "lower branch" increases, both effects almost compensating such that no pronounced variation of the valence band emission intensity is observed (cf. Fig. 1d, e). Good agreement between the experimental results and the one-step theory indicates the importance of coherent lattice scattering of the electron around this gap-like feature. We furthermore find that the semiclassical model also cannot account for the observed delays when neither the VB nor the W4f electrons coincide with the gap ($E_{\hbar\omega} = 117.1\,\mathrm{eV}$, $E_{\hbar\omega} = 124.4\,\mathrm{eV}$ and $E_{\hbar\omega} = 145\,\mathrm{eV}$). This indicates strong lattice scattering of the outgoing electron even far away from this region and furthermore confirms that any semiclassical treatment of the photoemission process

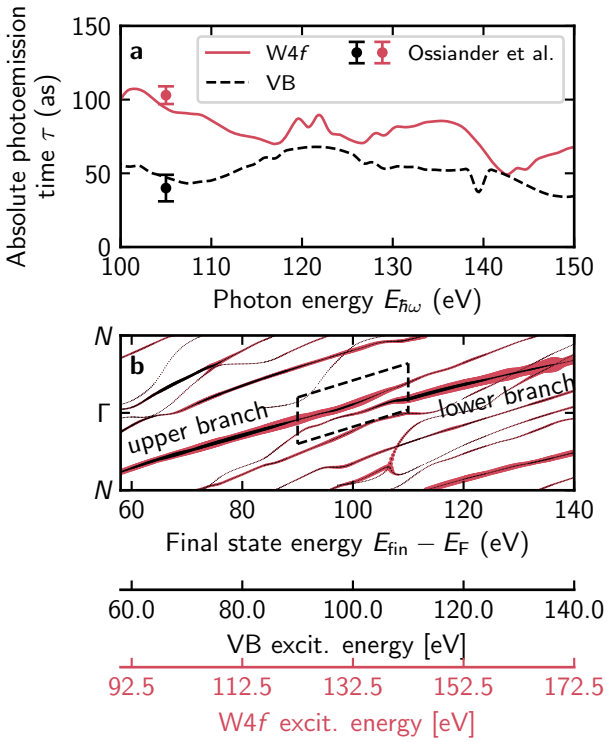

Figure 4: **Determination of the reference plane position and final state band structure.** **a** Calculated escape times for the W4f (solid red line) and the VB (dashed black line). Both curves exhibit strong variations with photon energy and no feature in the observed relative delay can be ascribed to the 4f or VB alone. In the calculation, the absolute values depend on the choice of the reference plane, which we determine from the absolute photoemission time reported for the W4f photoemission in [10]. We find good agreement of the calculation and the published absolute values (black data point) for a reference plane position 1.6 Å above the topmost layer of tungsten atoms. **b** Final-state band structure along ΓN for emission from the W4f (red) and 5d (black) states relative to the Fermi energy E_F calculated with a small optical potential of $V_i = 2$ eV at $k_{\|} = 0$ Å^{-1}. The thickness of the curve indicates the contribution to the photoelectron signal. The two extra axes below specify at which excitation energies the final states for the VB or 4f will coincide with the corresponding final states in **b**. It is apparent that at 103.1 eV and at 133.7 eV excitation energy the final states for the VB and 4f, respectively, fall into the region where the dominant conducting branch splits (marked by dashed box) into an "upper branch" (low energies) and a "lower branch" (high energies).

(cf. e.g. in [16, 17, 4]) is not adequate to capture the photoemission dynamics of the W(110) surface.

In the first photoemission timing experiment on the W(110) surface [4] a relative W4f-VB photoemission time delay of (110 ± 70) as was measured. Due to its large uncertainty it cannot readily be compared with the calculation here, although we note that the lower end of its error bars is close to the calculation in Fig. 2b.

In the calculation the escape time for both 4f and VB is determined with respect to a reference plane placed at a distance above the last layer of tungsten atoms. Its actual position is associated with the effective screening plane of the streaking laser field. Shifting this reference plane will result in a shift of the absolute escape times but will leave the relative time delay almost unaffected. We determine the position of the reference plane by matching the absolute photoemission times ($\tau_{4f} = (103 \pm 6)$ as and $\tau_{VB} = (40 \pm 9)$ as) reported in [10] at $E_{\hbar\omega} = 105$ eV independently for 4f and 5d emission, and find the best agreement with the plane positioned 1.6 Å (∼ 70% of the interlayer spacing) above the topmost layer of tungsten atoms, with a discrepancy of only 0.5 Å between the 4f and VB values. Best agreement with the relative delay times measured here is, however, found for a reference plane position of 5.1 Å above the topmost layer, which is used for the calculation shown in Fig. 2.

Finally, we want to comment on the discrepancies between the slope of the calculated relative delay

and the results of our spectrogram inversion at 103.1 eV and 133.7 eV (see Fig. 2). As noted above, these photon energies correspond to the final states of the VB and $4f$ electrons coinciding with the gap-like feature in the final state band structure. A numerical streaking experiment on a 1D model [18] revealed discrepancies between the streaking phase shift and EWS time delay around the band gaps, while in the nearly-free-electron regions the two values closely agreed. This was ascribed to a complicated interaction of the photoelectron wave packet with the laser field sharply screened at the surface, which is not included in the EWS theory. A fair comparison of EWS time delays and time shifts in streaking spectrograms requires the streaking to take place strictly after the photoelectron has completely traversed the surface barrier. The excited wave packets, however, have a finite spatial extent and while the abrupt decay of the streaking field across the surface [20] can warrant direct comparison of the EWS delay with results from attosecond streaking for spatially compressed wave packets, this no longer holds when the wave packets are distorted. A gap in the final state spectrum [30] or a strong energy dependence of the transition probability [33] have been identified as being responsible for such a distortion. Such a situation is encountered here around 103 eV where the emission jumps from the "upper branch" to the "lower branch" of the final state band structure, apparently causing a strong distortion of the outgoing wavepacket. Interestingly, the slope in the extracted delay differences leans in the same direction for both photon energies, indicating that photoelectrons excited from the VB and those excited from the $4f$ are affected in an opposite manner. Despite the mismatch in slope between the calculation and the ePIE results, it is important to that also in these cases we find good agreement for the central delays.

Conclusion

In summary, we report on photoemission timing measurements on the W(110) surface at photon energies exceeding 100 eV over a range of 50 eV via attosecond streaking spectroscopy. We find a variation in the relative photoemission time $\tau_{\mathrm{W}4f-\mathrm{VB}}$ between the W$4f$ and the valence band photoemission with photon energy that cannot be accounted for by semiclassical modeling, but is well-reproduced in the one-step theory of photoemission. We can directly relate the experimental results to the differences in Eisenbud-Wigner-Smith (EWS) time delays for the photoelectrons originating from the valence band and the W$4f$ states of tungsten (110), which closes a conceptual gap between the interpretation of photoemission timing experiments performed in atoms and molecules and on condensed matter. Using a spectrogram inversion algorithm, we access the slope of the excitation-dependent photoemission time, which we find to match the calculation well, with the exception of scenarios where the final state coincides with a gap-like feature in the final state band structure of the tungsten crystal. Our results indicate that even at high excitation energies a mechanistic interpretation of the photoemission dynamics is not possible and the observed time delays exhibit a complex behaviour, the interpretation of which requires microscopic *ab initio* theory capturing the full amplitude and phase information of the electron wave packet to grasp. Furhtermore, studying the distortion of the outgoing wave packet by time- and energy-resolved spectroscopy opens the door to novel investigations of the microscopic intricacies of light-matter interaction in the vicinity of a surface. Another viable approach to study surface effects in attosecond streaking is to introduce controlled changes to the screening scenario via surface adsorbates. In combination these approaches have the potential provide new insights into photochemistry and catalytic processes at surfaces.

References

[1] Karl Manne Georg Siegbahn, William Charles Price, and David Warren Turner. "A Discussion on photoelectron spectroscopy - Electron spectroscopy for chemical analysis (e.s.c.a.)" In: *Philosophical Transactions of the Royal Society of London. Series A, Mathematical and Physical Sciences* 268.1184 (1970), pp. 33–57. DOI: 10.1098/rsta.1970.0060. eprint: https://royalsocietypublishing.org/doi/pdf/10.1098/rsta.1970.0060. URL: https://royalsocietypublishing.org/doi/abs/10.1098/rsta.1970.0060.

[2] Andrea Damascelli. "Probing the electronic structure of complex systems by ARPES". In: *Physica Scripta* 2004.T109 (2004), p. 61.

[3] Jürgen Braun, Ján Minár, and Hubert Ebert. "Correlation, temperature and disorder: Recent developments in the one-step description of angle-resolved photoemission". In: *Physics Reports* 740 (2018). Correlation, temperature and disorder: Recent developments in the one-step description of angle-resolved photoemission, pp. 1–34. ISSN: 0370-1573. DOI: https://doi.org/10.1016/j.physrep.2018.02.007. URL: https://www.sciencedirect.com/science/article/pii/S0370157318300358.

[4] A. L. Cavalieri et al. "Attosecond spectroscopy in condensed matter". In: *Nature* 449.7165 (Oct. 2007), pp. 1029–1032. ISSN: 1476-4687. URL: https://doi.org/10.1038/nature06229.

[5] M. Schultze et al. "Delay in Photoemission". In: *Science* 328.5986 (2010), pp. 1658–1662. ISSN: 0036-8075. DOI: 10.1126/science.1189401. eprint: http://science.sciencemag.org/content/328/5986/1658.full.pdf. URL: http://science.sciencemag.org/content/328/5986/1658.

[6] Renate Pazourek, Stefan Nagele, and Joachim Burgdörfer. "Attosecond chronoscopy of photoemission". In: *Rev. Mod. Phys.* 87 (3 Aug. 2015), pp. 765–802. DOI: 10.1103/RevModPhys.87.765. URL: https://link.aps.org/doi/10.1103/RevModPhys.87.765.

[7] Zhensheng Tao et al. "Direct time-domain observation of attosecond final-state lifetimes in photoemission from solids". In: *Science* 353.6294 (2016), pp. 62–67. DOI: 10.1126/science.aaf6793. eprint: https://www.science.org/doi/pdf/10.1126/science.aaf6793. URL: https://www.science.org/doi/abs/10.1126/science.aaf6793.

[8] Cong Chen et al. "Distinguishing attosecond electron–electron scattering and screening in transition metals". In: *Proceedings of the National Academy of Sciences* 114.27 (2017), E5300–E5307. DOI: 10.1073/pnas.1706466114. eprint: https://www.pnas.org/doi/pdf/10.1073/pnas.1706466114. URL: https://www.pnas.org/doi/abs/10.1073/pnas.1706466114.

[9] Reto Locher et al. "Energy-dependent photoemission delays from noble metal surfaces by attosecond interferometry". In: *Optica* 2.5 (May 2015), pp. 405–410. DOI: 10.1364/OPTICA.2.000405. URL: https://opg.optica.org/optica/abstract.cfm?URI=optica-2-5-405.

[10] M. Ossiander et al. "Absolute timing of the photoelectric effect". In: *Nature* 561.7723 (Sept. 2018), pp. 374–377. ISSN: 1476-4687. URL: https://doi.org/10.1038/s41586-018-0503-6.

[11] M. Isinger et al. "Photoionization in the time and frequency domain". In: *Science* 358.6365 (2017), pp. 893–896. DOI: 10.1126/science.aao7043. eprint: https://www.science.org/doi/pdf/10.1126/science.aao7043. URL: https://www.science.org/doi/abs/10.1126/science.aao7043.

[12] J. Benda, Z. Mašín, and J. D. Gorfinkiel. "Analysis of RABITT time delays using the stationary multiphoton molecular R-matrix approach". In: *Phys. Rev. A* 105 (5 May 2022), p. 053101. DOI: 10.1103/PhysRevA.105.053101. URL: https://link.aps.org/doi/10.1103/PhysRevA.105.053101.

[13] S Nagele et al. "Time-resolved photoemission by attosecond streaking: extraction of time information". In: *Journal of Physics B: Atomic, Molecular and Optical Physics* 44.8 (Apr. 2011), p. 081001. DOI: 10.1088/0953-4075/44/8/081001. URL: https://dx.doi.org/10.1088/0953-4075/44/8/081001.

[14] Johann Riemensberger et al. "Attosecond Dynamics of *sp*-Band Photoexcitation". In: *Phys. Rev. Lett.* 123 (17 Oct. 2019), p. 176801. DOI: 10.1103/PhysRevLett.123.176801. URL: https://link.aps.org/doi/10.1103/PhysRevLett.123.176801.

[15] Lamia Kasmi et al. "Effective mass effect in attosecond electron transport". In: *Optica* 4.12 (Dec. 2017), pp. 1492–1497. DOI: 10.1364/OPTICA.4.001492. URL: https://opg.optica.org/optica/abstract.cfm?URI=optica-4-12-1492.

[16] S. Heinrich et al. "Attosecond intra-valence band dynamics and resonant-photoemission delays in W(110)". In: *Nature Communications* 12.1 (June 2021), p. 3404. ISSN: 2041-1723. URL: https://doi.org/10.1038/s41467-021-23650-7.

[17] C. Lemell et al. "Simulation of attosecond streaking of electrons emitted from a tungsten surface". In: *Phys. Rev. A* 79 (6 June 2009), p. 062901. DOI: 10.1103/PhysRevA.79.062901. URL: https://link.aps.org/doi/10.1103/PhysRevA.79.062901.

[18] R. O. Kuzian and E. E. Krasovskii. "One-step theory of photoelectron escape time: Attosecond spectroscopy of Mg(0001)". In: *Phys. Rev. B* 102 (11 Sept. 2020), p. 115116. DOI: 10.1103/PhysRevB.102.115116. URL: https://link.aps.org/doi/10.1103/PhysRevB.102.115116.

[19] E. Magerl et al. "A flexible apparatus for attosecond photoelectron spectroscopy of solids and surfaces". In: *Review of Scientific Instruments* 82.6 (2011), p. 063104. DOI: 10.1063/1.3596564. eprint: https://doi.org/10.1063/1.3596564. URL: https://doi.org/10.1063/1.3596564.

[20] S. Neppl et al. "Direct observation of electron propagation and dielectric screening on the atomic length scale". In: *Nature* 517.7534 (Jan. 2015), pp. 342–346. ISSN: 1476-4687. URL: https://doi.org/10.1038/nature14094.

[21] R. Kienberger et al. "Atomic transient recorder". In: *Nature* 427.6977 (Feb. 2004), pp. 817–821. ISSN: 1476-4687. URL: https://doi.org/10.1038/nature02277.

[22] V. S. Yakovlev et al. "Attosecond Streaking Enables the Measurement of Quantum Phase". In: *Phys. Rev. Lett.* 105 (7 Aug. 2010), p. 073001. DOI: 10.1103/PhysRevLett.105.073001. URL: https://link.aps.org/doi/10.1103/PhysRevLett.105.073001.

[23] Alexander Guggenmos et al. "Chromium/scandium multilayer mirrors for isolated attosecond pulses at 145 eV". In: *Opt. Lett.* 40.12 (June 2015), pp. 2846–2849. DOI: 10.1364/OL.40.002846. URL: https://opg.optica.org/ol/abstract.cfm?URI=ol-40-12-2846.

[24] A. Abrami et al. "Super ESCA: First beamline operating at ELETTRA". In: *Review of Scientific Instruments* 66.2 (1995), pp. 1618–1620. DOI: 10.1063/1.1145862. eprint: https://doi.org/10.1063/1.1145862. URL: https://doi.org/10.1063/1.1145862.

[25] S. Neppl et al. "Attosecond Time-Resolved Photoemission from Core and Valence States of Magnesium". In: *Phys. Rev. Lett.* 109 (8 Aug. 2012), p. 087401. DOI: 10.1103/PhysRevLett.109.087401. URL: https://link.aps.org/doi/10.1103/PhysRevLett.109.087401.

[26] J. Gagnon, E. Goulielmakis, and V. S. Yakovlev. "The accurate FROG characterization of attosecond pulses from streaking measurements". In: *Applied Physics B* 92.1 (July 2008), pp. 25–32. ISSN: 1432-0649. URL: https://doi.org/10.1007/s00340-008-3063-x.

[27] M. Lucchini et al. "Light-Matter Interaction at Surfaces in the Spatiotemporal Limit of Macroscopic Models". In: *Phys. Rev. Lett.* 115 (13 Sept. 2015), p. 137401. DOI: 10.1103/PhysRevLett.115.137401. URL: https://link.aps.org/doi/10.1103/PhysRevLett.115.137401.

[28] Y. Mairesse and F. Quéré. "Frequency-resolved optical gating for complete reconstruction of attosecond bursts". In: *Phys. Rev. A* 71 (1 Jan. 2005), p. 011401. DOI: 10.1103/PhysRevA.71.011401. URL: https://link.aps.org/doi/10.1103/PhysRevA.71.011401.

[29] M. Lucchini et al. "Ptychographic reconstruction of attosecond pulses". In: *Opt. Express* 23.23 (Nov. 2015), pp. 29502–29513. DOI: 10.1364/OE.23.029502. URL: https://opg.optica.org/oe/abstract.cfm?URI=oe-23-23-29502.

[30] E. E. Krasovskii. "Attosecond spectroscopy of solids: Streaking phase shift due to lattice scattering". In: *Phys. Rev. B* 84 (19 Nov. 2011), p. 195106. DOI: 10.1103/PhysRevB.84.195106. URL: https://link.aps.org/doi/10.1103/PhysRevB.84.195106.

[31] C.-H. Zhang and U. Thumm. "Effect of wave-function localization on the time delay in photoemission from surfaces". In: *Phys. Rev. A* 84 (6 Dec. 2011), p. 065403. DOI: 10.1103/PhysRevA.84.065403. URL: https://link.aps.org/doi/10.1103/PhysRevA.84.065403.

[32] C. N. Berglund and W. E. Spicer. "Photoemission Studies of Copper and Silver: Theory". In: *Phys. Rev.* 136 (4A Nov. 1964), A1030–A1044. DOI: 10.1103/PhysRev.136.A1030. URL: https://link.aps.org/doi/10.1103/PhysRev.136.A1030.

[33] E. E. Krasovskii et al. "Rapid propagation of a Bloch wave packet excited by a femtosecond ultraviolet pulse". In: *Phys. Rev. B* 94 (19 Nov. 2016), p. 195434. DOI: 10.1103/PhysRevB.94.195434. URL: https://link.aps.org/doi/10.1103/PhysRevB.94.195434.

[34] U. Becker et al. "Subshell photoionization of Xe between 40 and 1000 eV". In: *Phys. Rev. A* 39 (8 Apr. 1989), pp. 3902–3911. DOI: 10.1103/PhysRevA.39.3902. URL: https://link.aps.org/doi/10.1103/PhysRevA.39.3902.

[35] A. Herrera-Gomez et al. “Practical methods for background subtraction in photoemission spectra”. In: *Surface and Interface Analysis* 46.10-11 (2014), pp. 897–905. DOI: https://doi.org/10.1002/sia.5453. eprint: https://analyticalsciencejournals.onlinelibrary.wiley.com/doi/pdf/10.1002/sia.5453. URL: https://analyticalsciencejournals.onlinelibrary.wiley.com/doi/abs/10.1002/sia.5453.

[36] Christian Brunner et al. “Deep learning in attosecond metrology”. In: *Opt. Express* 30.9 (Apr. 2022), pp. 15669–15684. DOI: 10.1364/OE.452108. URL: https://opg.optica.org/oe/abstract.cfm?URI=oe-30-9-15669.

[37] E. E. Krasovskii, F. Starrost, and W. Schattke. “Augmented Fourier components method for constructing the crystal potential in self-consistent band-structure calculations”. In: *Phys. Rev. B* 59 (16 1999), pp. 10504–10511. DOI: 10.1103/PhysRevB.59.10504. URL: http://link.aps.org/doi/10.1103/PhysRevB.59.10504.

[38] E. E. Krasovskii. “Augmented-plane-wave approach to scattering of Bloch electrons by an interface”. In: *Phys. Rev. B* 70 (24 2004), p. 245322. DOI: 10.1103/PhysRevB.70.245322. URL: http://link.aps.org/doi/10.1103/PhysRevB.70.245322.

[39] E. E. Krasovskii and W. Schattke. “Surface electronic structure with the linear methods of band theory”. In: *Phys. Rev. B* 56 (20 1997), pp. 12874–12883. DOI: 10.1103/PhysRevB.56.12874. URL: http://link.aps.org/doi/10.1103/PhysRevB.56.12874.

[40] E. E. Krasovskii. “Accuracy and convergence properties of the extended linear augmented-plane-wave method”. In: *Phys. Rev. B* 56 (20 Nov. 1997), pp. 12866–12873. DOI: 10.1103/PhysRevB.56.12866. URL: https://link.aps.org/doi/10.1103/PhysRevB.56.12866.

Methods

Sample preparation. The clean W(110) surface was prepared by a well established procedure including Ar^+ ion sputtering followed by repeated oxidation/annealing cycles in a $2 \cdot 10^{-6}$ mbar oxygen atmosphere. The final surface preparation step is a 10-20s flash annealing to 2400 K in UHV. Surface crystallinity and cleanliness is verified by stationary (AlKα radiation) X-ray photoelectron spectroscopy (XPS), low-energy electron diffraction (LEED) and high-resolution photoelectron spectroscopy at the synchrotron facility ELLETRA (Trieste, Italy).

Photon energy calibration. The 145 eV mirror was characterized using X-ray reflectometry at the Physikalisch Technische Bundesanstalt (PTB) beamline at the BESSY II synchrotron facility in Berlin [23]. The other mirrors have been calibrated via the direct photoemission from the Xe4*d* core-levels as depicted in Extended Data Fig. . The well-known doublet is split into two components ($\frac{5}{2}$ at $E_{\text{bind}} = 67.5\,\text{eV}$ and $\frac{3}{2}$ at $E_{\text{bind}} = 69.5\,\text{eV}$). The NOO Auger-Meitner emission is used to verify the kinetic energy calibration of the time-of-flight (TOF) spectrometer. The central photon energies $E_{\hbar\omega}$ and bandwidths $\Delta\omega$ are determined via a least-squares Gaussian fit to the Xe4*d* signal taking their energy-dependent cross-sections [34] into account.

Photoemission time delay extraction. Attosecond streaking delays are extracted with the method introduced in [5, 25]. The strong-field solution to the time-dependent Schrödinger equation is subjected to the wavepacket appxoximation (WPA) and central momentum approximation (CMA) [22] and used to parametrize a spectrogram $P_{\text{fit}}(E_{\text{kin}}, \Delta\tau)$ in terms of the NIR vector potential $A_L(t)$ and photoelectron wavepackets $\chi_{i_q}(t)$

$$\chi_{i_q}(t) = \mathcal{F}^{-1}\left\{ a_{i_q} \cdot e^{-4\ln(2)\left(\omega-\omega_X-E_{B,i_q}\right)^2/\Delta\omega_X^2} \cdot e^{-i\frac{i}{2}\beta_X\left(\omega-\omega_X-E_{B,i_q}\right)^2} \right\},$$
$$A_L(t) = A_0 \cdot e^{-4\ln(2)t^2/t_L^2} \cdot \sin\left(\omega_L t + \frac{1}{2}\beta_L t^2 + \Phi_{CE}\right), \tag{3}$$

whereby the solution space for the problem of inverting the spectrogram is restricted. Therefore this analysis method is referred to as rTDSE method. Photoemission spectra are modeled as comprised of effective bound states a_{i_q} such that the static spectra measured with isolated attosecond pulses are reproduced in shape well as shown in fig. S2 with initial values for the fitting of their relative positions and intensities inferred from the high-resolution synchrotron data. Initial values are given in Extended Data Table 1. The spectral and temporal phases of the wave packets and NIR pulses are carried up to second order (β_X, β_L) in the fitting process.

The best fit photoemission spectrogram $P_{fit}(E_{kin}, \Delta\tau)$ follows as

$$\min_{\omega_X,\beta_X,a_q,A_0,t_L,\omega_L,\beta_L,\Phi_{CE}} \left|\left| \frac{\partial}{\partial(\Delta\tau)} P(E_{kin},\Delta\tau) - \frac{\partial}{\partial(\Delta\tau)} P_{fit}(E_{kin},\Delta\tau) \right|\right|^2 \tag{4}$$
$$P_{fit}(E_{kin},\Delta\tau) = \sum_q^Q a_q \sum_{i_q}^{N_q} \left| a_{i_q} \int_{-\infty}^{\infty} dt\, \chi_{i_q}(t+\Delta\tau) \cdot e^{-i\Phi_V(t;p_{i_q})} \right|^2,$$
$$\Phi_V\left(t;p_{i_q}\right) = \int_t^{\infty} dt' \left(p_{i_q} - eA_L(t')\right)^2, \tag{5}$$

where $\Phi_V(t)$ denotes the Volkov phase and p_{i_q} the photoelectron momentum along the surface normal, respectively. Fitting is perfromed with the Levenberg-Marquardt algorithm. Taking the partial derivative along the delay-axis of the spectrograms while fitting ensures that any incoherent background which does not vary with delay time vanishes. Thereby no assumption about the shape of the inelastic background is made and experimenter influence in the rTDSE analysis is reduced.

A total of 569 spectrograms were analyzed. The resulting delay values are sufficiently normal-distributed warranting reporting their average as a single-valued relative photoemission delay and the standard error $\tau_{\text{err}} = 1.96\sigma/\sqrt{N}$ as uncertainty. Figure 3 gives an overview over the statistics. At the sacrifice of a significant part of the photoelectron count rate the TOF detector can be set to a small acceptance angle. A subset of the measurements were taken this way to test that the angular integration does not significantly changes the time delay. The respective statistics are shown in fig. S4.

Ptychographic spectrogram inversion and "wave packet" reconstruction. Starting point is again the strong-field solution to the time-dependent Schrödinger equation subjected to WPA and CMA. The expression for the spectrogram due to a single photoelectron wave packet $\chi(t)$ takes the form

$$P(E_{\mathrm{kin}}, \Delta\tau) = \left|\mathcal{F}\left\{\chi(t+\Delta\tau)G(t,p_0)\right\}\right|^2, \tag{6}$$

where $G(t,p_0)$ encodes the NIR pulse's vector potential. In our range of parameters the streaking features due to the VB and W4f photoemission are well approximated by above expression after background subtraction via the Shirley-Proctor-Sherwood method (cf. [35]). An experimental spectrogram is split apart into two separate spectrograms, one for the VB and one for the W4f, each of which can be subjected to the extended ptychographic iterative engine (ePIE) [29] for the retrieval of "wave packets" $\chi_{\mathrm{VB}}(t)$ and $\chi_{\mathrm{W}4f}(t)$ and the NIR field via the functions $G(t,p_0^{\mathrm{VB}})$ and $G(t,p_0^{\mathrm{W}4f})$ respectively. We enforce consistency by averaging the NIR pulses resulting from each iteration of the VB and W4f retrieval and feeding them back into the next iteration. This enables us to retrieve different 'wave packets' streaked by the same NIR pulse. In order to stabilize the algorithm against walk-off of the 'wave packets' or the NIR pulse we cycle through the individual photoelectron spectra comprising each spectrogram in random order in each iteration. We freeze updating the gate functions $G(t,p_0^{\mathrm{VB}})$ and $G(t,p_0^{\mathrm{W}4f})$ after a certain number of iterations to ensure proper convergence of the 'wave packets'. Further details of our implementation are given in [36].

The ePIE can only be applied to spectrograms where the streaking amplitude is sufficiently small as to ensure that the VB and W4f streaking features do not intersect energetically. This is not problematic due to their large energetic separation though. However, even then for some spectrograms the algorithm does not converge to a meaningful result, usually seen by the NIR pulse taking an un-physical shape.

In total 540 spectrograms were processed successfully. The complex valued 'wave packets' are fourier transformed to obtain their spectrum and then cast into their polar representation

$$\chi(E) = |S(E)| \exp\left(i\varphi(E)\right). \tag{7}$$

The VB and W4f 'wave packet' for each scan are aligned on the energy axis such that the maxima of their spectra $|S_i(E)|^2$ coincide. Then, the relative photoemission delay is determined as

$$\tau_{\mathrm{W}4f-\mathrm{VB}}(E) = \frac{\partial}{\partial E}\left(\varphi_{\mathrm{W}4f}(E) - \varphi_{\mathrm{VB}}(E)\right). \tag{8}$$

The photoemission time delays are then averaged pointwise whereby also a standard deviatin $\sigma(E)$ can be defined. Uncertainties are again reported as $\tau_{\mathrm{err}}(E) = 1.96\sigma(E)/\sqrt{N}$. The relative delay $\tau_{\mathrm{W}4f-\mathrm{VB}}(E)$ can only meaningfully be defined where the $|S_i(E)|^2$ attain appreciable values. As the bandwidths of our multilayer XUV optics range from 3.5 eV to 4.6 eV we choose an interval of ± 2.5 eV around the energetic center. Figure shows the number of scans successfully evaluated per photon energy.

Photoemission delay extraction in the vicinity of a band gap. In the main text we attribute the large mismatch in curvature between ePIE and the one-step calculation to the gap-like structure in the final-state band structure around 103 eV above the Fermi energy. In order to test this we re-evaluated a numerical streaking experiment on a one-dimensional model crystal (origial publication in [33]) with ePIE and the rTDSE method. The model crystal exhibits an energy gap which is hit by its 'core-level' ($E_{\mathrm{bind}} = 41.2$ eV) photoemission at around 80 eV photon energy. While no energy gap in this sense exists for the W(110) surface it has been pointed out that a strong distortion of the wave packet is to be expected whenever the energy of the wave packet approaches an intensity minimum. As stated in the main text, the switch between the "upper" and "lower" branch of the final-state band structure carrying the photocurrent constitutes such a situation, and the behaviour of the photoemission time delay around this region is expected to share the same peculiarities. We therefore evaluate the results of the 1D model which is expected to give qualitatively comparabe results from which the same conclusions can be drawn.

We apply both delay extraction methods also used for the experimental results to the calculated spectrograms and compare them with the center-of-energy analysis published in [33] (top panel in Extended Data Fig.). It is easily seen that the ePIE results strongly resemble the the center-of-energy analysis but yield a more drastic curvature around the band-gap. Furthermore, it should be

noted that the individial ePIE delay curves for each spectrogram for adjacent photon energies mostly overlap which demonstrates that ePIE can in fact assess the photoemission dynamics in a small region around the central energy where a spectrogram is recorded, but overestimates the slope around the band gap. Furthermore, we find that the rTDSE results do not agree with the other methods in the vicinity of the gap. We attribute this to the spectrogram separating into effectively two traces directly on-bandgap in the 1D model which the rTDSE method cannot handle correctly (see lower panels in Extended Data Fig.). Still, we find ePIE to overestimate the the delay around the gap.

Computational details. In the *ab initio* calculation of photoemission from W(110) both initial and final states are eigenfunctions of a density-functional Hamiltonian (in local density approximation, LDA) with a realistic potential both in the bulk and at the surface, including the Z/r singularity at the nuclei. Spin-orbit is included as the second variation. The crystal potential $V(\mathbf{r})$ is obtained with a self-consistent full-potential augmented plane waves method [37]. For the final states, the inelastic scattering is included by adding a spatially constant imaginary potential $-iV_{\rm i}(E)$ to the potential $V(\mathbf{r})$ in the crystal half-space. Its energy dependence is taken to be an extrapolation of five points calculated as the expectation value of the imaginary part of the self-energy operator in the GW approximation, see Fig. 1(c) in ref. [33].

In the LDA, the binding energies of the $4f$ band are underestimated by 3.7 eV. In calculating excitation energies, the experimental location of the $4f$ band is adopted. No correction is introduced for the valence band. The effect of the real part of self-energy for the final states was simulated by applying the linear transformation $E \to 1.03 \cdot E$.

The LEED states are obtained with the embedding technique [38], in which the bulk of the semi-infinite W(110) crystal is represented by it complex band structure [39] and the surface by a stand-alone three-layer W(110) slab. The computational scheme is presented in Extended Data Fig. 7. In the context of LEED, the electron is incident from the right, and the half-space $z < z_{\rm L}$ contains only transmitted Bloch waves. In the embedded region $z_{\rm L} \le z \le z_{\rm R}$ an all-electron representation of $\Psi_{\rm f}(\mathbf{r})$ is obtained in terms of augmented plane waves with an extended radial basis set [40]. The right vacuum half-space $z > z_{\rm R}$ contains the incident wave and reflected waves. The representation of the LEED state in terms of the surface reciprocal lattice vectors $\mathbf{G}_{\|}$ reads

$$\Psi_{\rm f}(\mathbf{r}_{||}, z) = \sum_{\mathbf{G}_{\|}} \phi_{\mathbf{G}_{\|}}(z) \exp[i(\mathbf{k}_{||} + \mathbf{G}_{\|})\, \mathbf{r}_{||}].$$

Figure 7 illustrates that in the crystal the contribution from the $\mathbf{G}_{\|} \neq 0$ Fourier harmonics strongly exceeds the $\mathbf{G}_{\|} = 0$ contribution, which points to the fact that a one-dimensional or a free-electron approximation for the final state is insufficient. At the same time, the good agreement between the black and the green curve in Extended Data Fig. 7(b) shows that the step-like approximation for the surface barrier is quite reasonable in the present case, so one may expect the results to be not too sensitive to the details of the potential at the surface.

Semiclassical escape time and position of the reference plane. A detailed account of the one-step calculations is given in [18]. Supplemental results to what is presented in the main text are given here. The optical potential used in the one-step calculations and the accompanying semiclassical escape time are shown in Extended Data Fig. .

Position of the reference plane. We extrapolated the position of the reference D plane above the topmost layer of tungsten atoms by calculating the escape time for multiple values of D and comparing them to the results for the absolute photoemission time reported by Ossiander et al. in [10]. The results of the extrapolation are shown in Extended Data Fig. 9

Delay differences for the W$4f_{\frac{5}{2}}$ and W$4f_{\frac{7}{2}}$ initial states. The spin-orbit splitting of the W$4f$ photoemission into the W$4f_{\frac{5}{2}}$ and W$4f_{\frac{7}{2}}$ is not resolved in the experiment due to the large bandwidth of the XUV pulses. Extended Data Fig. 10 shows these components resolved in the calculation. We do not find any significant differences between the two curves beyond their shift in enery. Therefore we use their average in the main text.

Valence band photoemission of the W(110) surface. Extended Data Fig. 11 shows a high resolution photoelectron spectrogram recorded at SuperESCA in which the characteristic features of

the W(110) valence photoemission can be seen. The $5d$ band is too weak in its photoelectron signal to contribute significantly to the attosecond delays presented in our study.

Data availability. The data that support the findings of this study are available from the corresponding authors upon reasonable request.

Code availability. The data analysis code is available from the corresponding authors upon reasonable request.

Acknowledgements

We thank Alexander Guggenmos for his contributions to the developement of the XUV reflectors used in this work and Daniel Lizzit for his support during the measurements at SuperESCA.

C. S. implemented the ptychographic reconstruction algorithm, analyzed the data, prepared the figures and wrote the original draft. J. R. analyzed the data. J. R., M. O. , D. P., A. A., A. C., S. N., R. E., W. H., M. J., M. G., E. B., A. K., K. H. and M. S. performed experiments and reviewed the manuscript. E. K. and Ro. K. developed the numerical methods, performed calculations and reviewed the manuscript. L. B. and S. L. supported the experiment at the SuperESCA beamline and reviewed the manuscripts. Jü. B., H. E. and J. M. provided valuable insights and reviewed the manuscript. U. K. supplied multilayer XUV reflectors and reviewed and discussed the manuscript. D. M., Jo. B., F. A., P. F. and Re. K. supervised the study and reviewed the manuscript.

Financial support from the Spanish Ministry of Science and Innovation (MICINN, Grant No. PID2019-105488GB-I00) is acknowledged. We furthermore acknowledge funding from Deutsche Forschungsgemeinschaft (DFG, German Research Foundation) under Germany's Excellence Strategy – EXC 2089/1 – 390776260 (e-conversion) and an ERC Consolidator Grant, ERC-CoG-2014, ID: 647695 (AEDMOS).

Conflicts of interest. The authors declare no conflicts of interest.

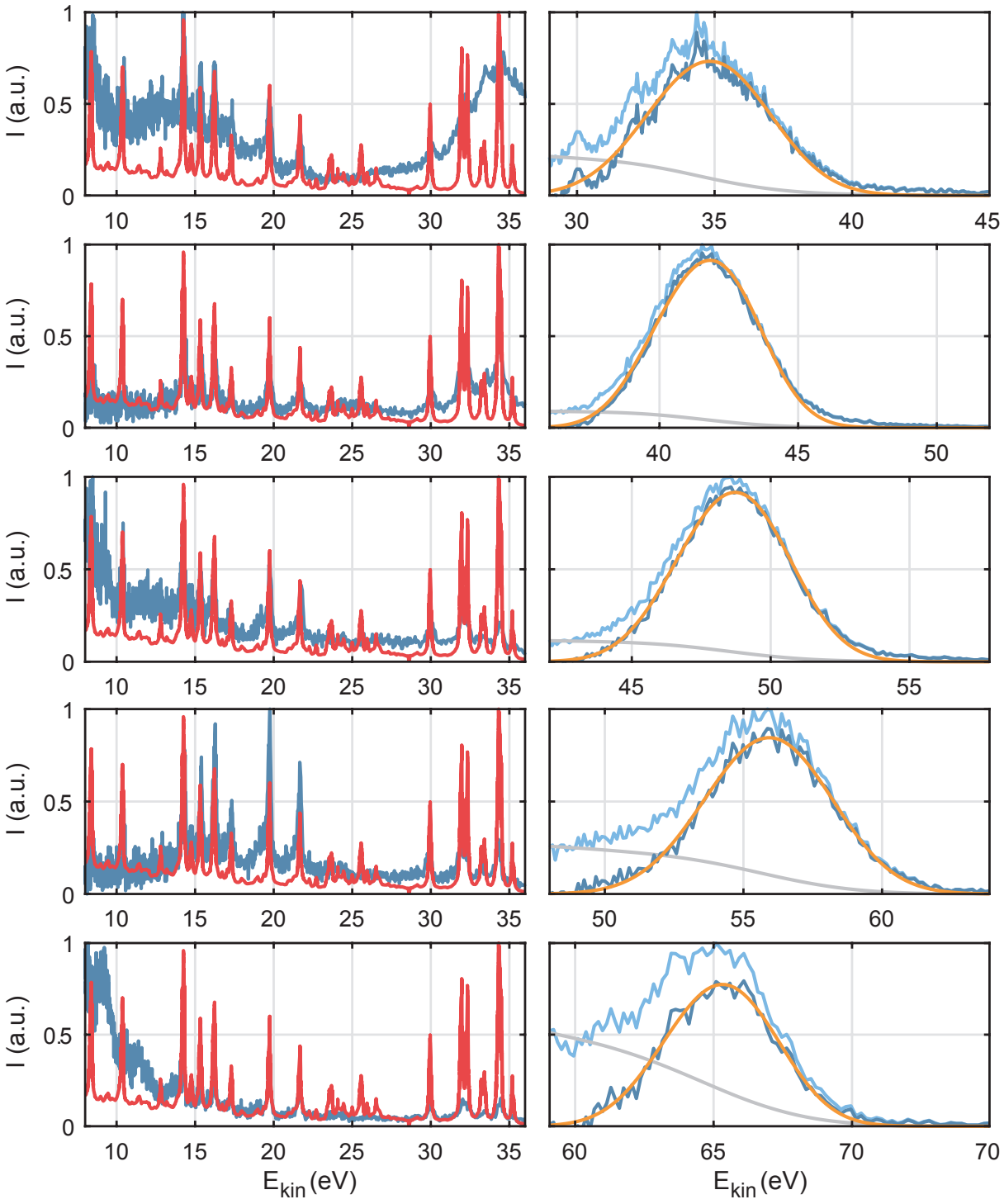

Extended Data Figure 1: Calibration of the XUV multilayers via the Xe4*d* photoemission. Left panels depict the Xe NOO Auger-Meitner signal (red from literature [34] and blue as measured) used to verify the kinetic energy calibration of the TOF detector, right panels show the Xe4*d* photoelectron signal with the photon energies 103.1 eV, 103.1 eV, 110.1 eV, 117.1 eV, 124.4 eV and 133.7 eV from top to bottom. Light blue is the spectrum before background (gray) subtraction, dark blue is after. The fit is shown in orange.

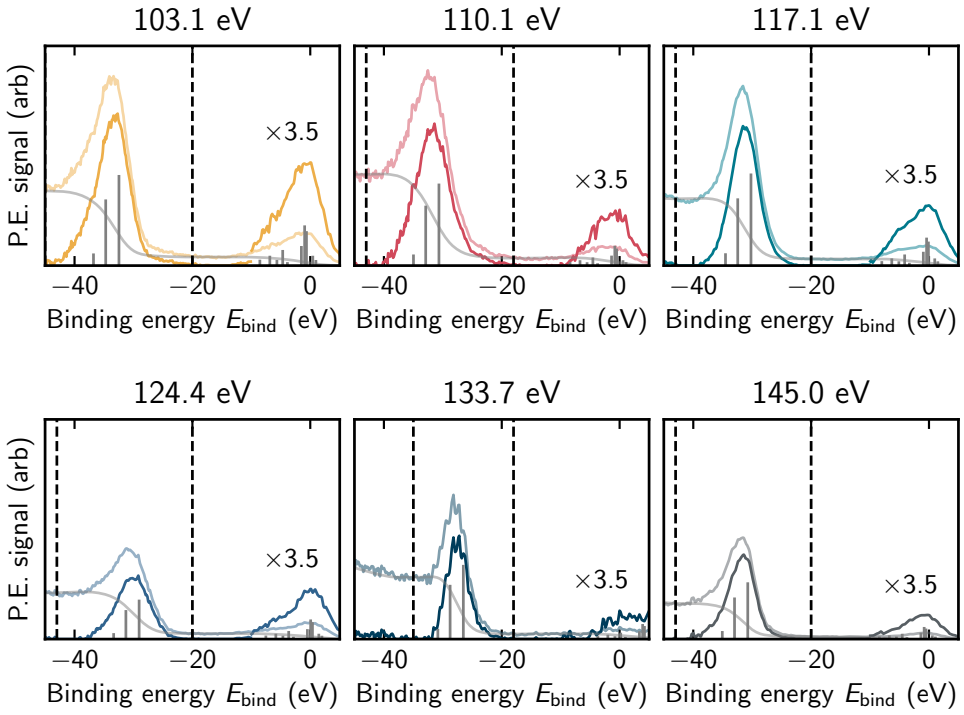

Extended Data Figure 2: Definition of incoherent components for the rTDSE retrieval algorithm for relevant photon energies. Static photoemission spectra recorded with isolated attosecond pulses between 103.1 eV and 145 eV. The as measured spectra are plotted in light coloring and after background subtraction with a employing a piecewise Shirley-Proctor-Sherwood-background (black dashed lines indicate points between which the background is defined) in dark coloring. The background is shown in light gray. Gray vertical bars indicate the individual incoherent contributions to VB and W4f respectively.

Extended Data Table 1: Initial-value binding energies and relative intensities of the effective bound states for the rTDSE delay extraction

W4f	$E_{\mathrm{B},1_q}$ (eV)	Intensity a_{1_q} (arb.)
	31.25	1.00
	33.50	0.73
	35.58	0.12
VB	$E_{\mathrm{B},2_q}$ (eV)	Intensity a_{2_q} (arb.)
	−0.85	0.02
	−0.33	0.03
	0.75	0.13
	1.05	0.16
	1.61	0.07
	3.98	0.01
	4.78	0.06
	5.76	0.02
	6.96	0.03
	8.65	0.02

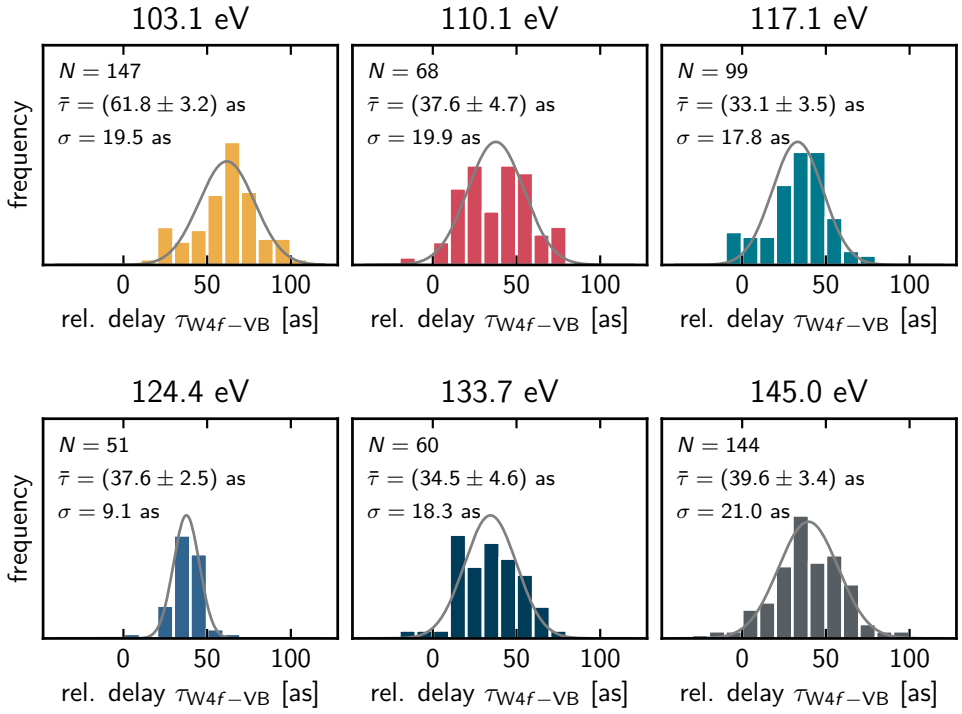

Extended Data Figure 3: Statistical analysis of the rTDSE delays. The relative delays extracted with the rTDSE method are sufficiently normal-distributed whereby their average and standard error can be meaningfully reported.

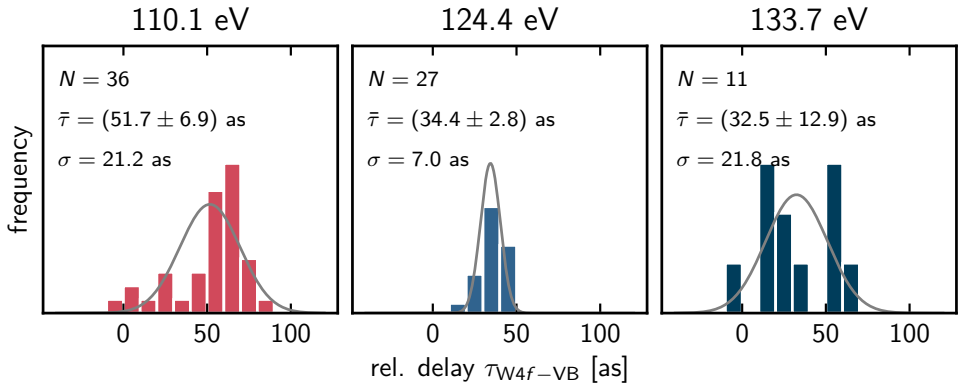

Extended Data Figure 4: Statistical analysis of the rTDSE delays for the small acceptance angle of ±2°. Only at 110.1 eV we find a difference between the full dataset (cf. fig. 3) and the subset outside their respective uncertainties.

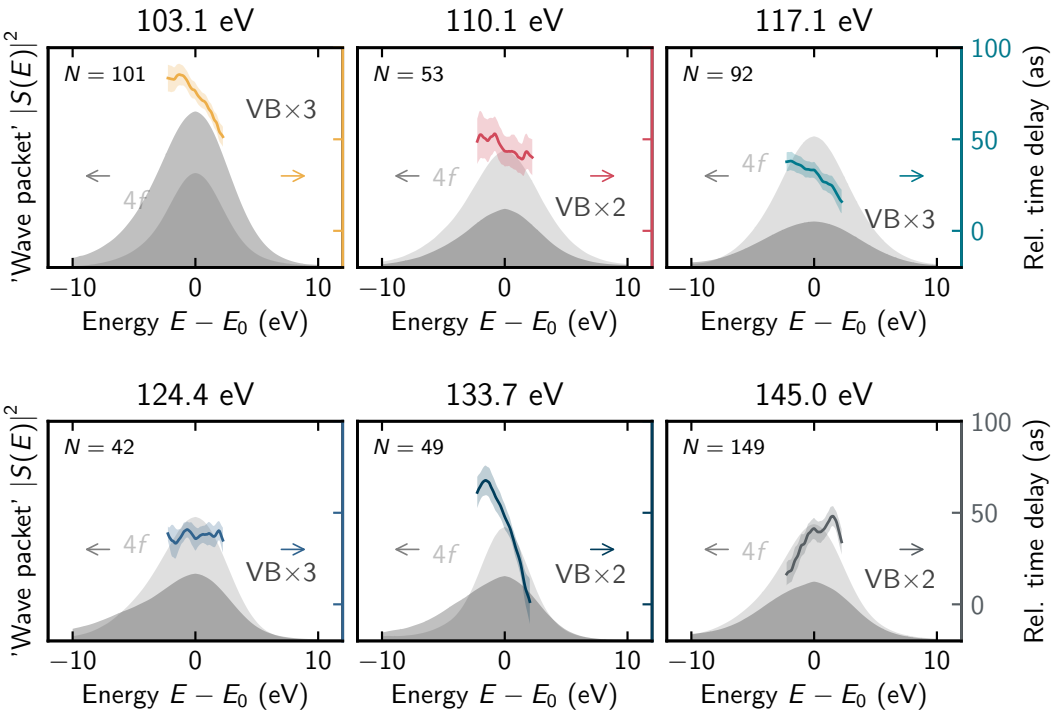

Extended Data Figure 5: Overview over the ePIE analysis with the number of scans successfully evaluated per photon energy.

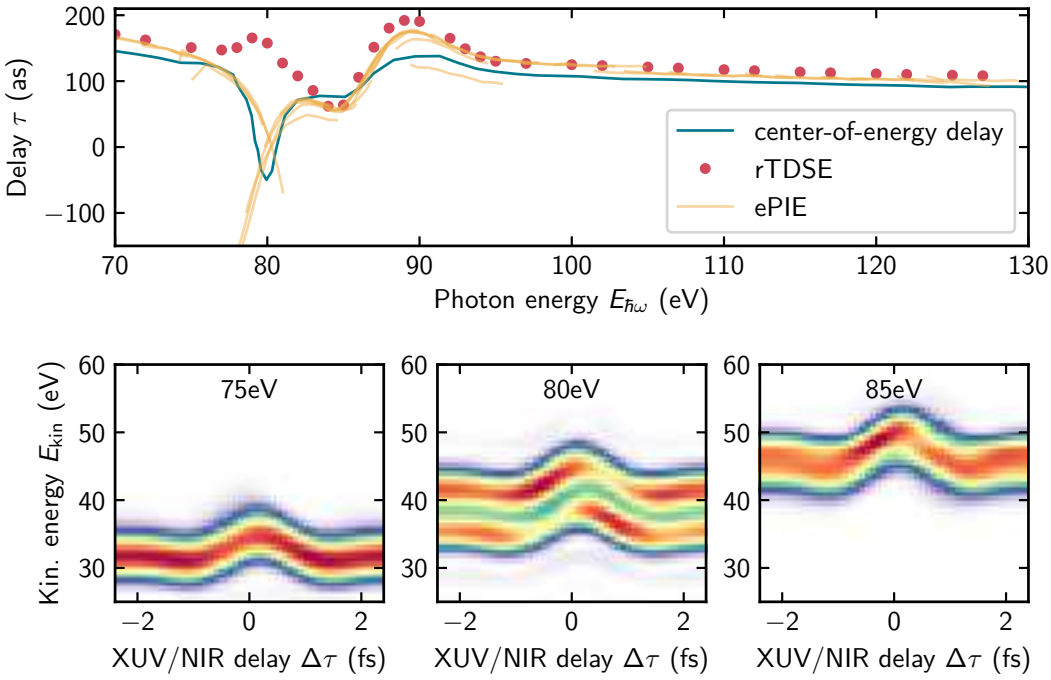

Extended Data Figure 6: Delay extraction across a band-gap in the final state spectrum. On-gap ($E_{\hbar\omega} = 80\,\mathrm{eV}$) ePIE (yellow curves) overestimates the slope of the time delay. Generally though, the shape of the center-of-energy (COE) result is reproduced well with the individual curves mostly overlapping. This demonstrates the fitness of ePIE to assess photoemission timing in a small area around its cenral energy. The rTDSE method cannot properly handle the spectrogram essentially decomposing into two traces on-gap correctly, resulting in the disagreement between COE, ePIE and rTDSE at $E_{\hbar\omega} = 80\,\mathrm{eV}$.

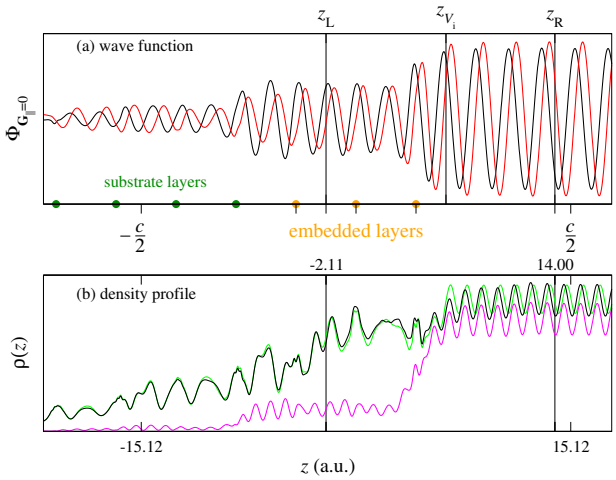

Extended Data Figure 7: Computational scheme to calculate the full-potential time-reversed LEED function Ψ_f in Eq. (1) of the main text. (a) $\mathbf{G}_\parallel = 0$ component of $\Psi_\mathrm{f}(\mathbf{r})$ for normal emission at $E - E_\mathrm{F} = 103$ eV: Re $\phi_0(z)$ (black) and Im $\phi_0(z)$ (red). Green circles show the W(110) substrate layers and orange circles are the stand-alone three-layer slab used to obtain the crystal potential in the surface layers. The artificial supercell, whose eigenfunctions are used to represent Ψ_f between z_L and z_R, extends from $-c/2$ to $c/2$, with the supercell lattice constant $c = 30.2$ a.u.. z_{V_i} is the onset of the optical potential. (b) Probability density profile $\rho(z) = \int |\Psi_\mathrm{f}(\mathbf{r}_{||}, z)|^2 \, d\mathbf{r}_{||}$. Black line is the total density and magenta line is the $\mathbf{G}_\parallel = 0$ contribution $|\phi_0(z)|^2$. Green line is $\rho(z)$ for a step-like potential that abruptly changes from the bulk distribution to the vacuum level at z_{V_i}.

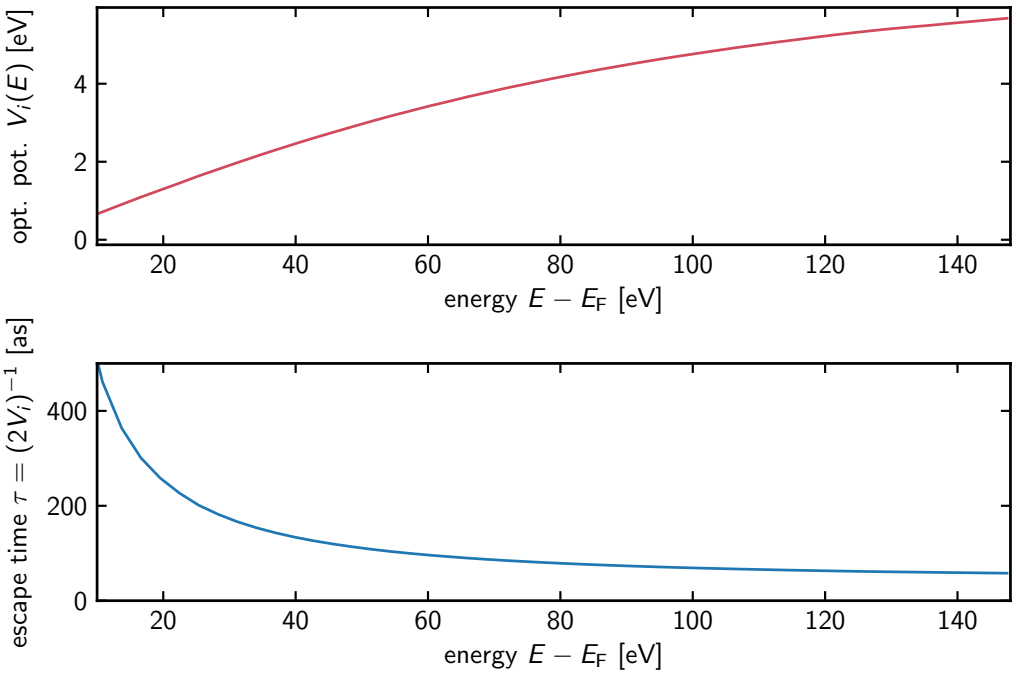

Extended Data Figure 8: Optical potential $V_i(E)$ (top panel) and resulting semiclassical escape time (bottom panel).

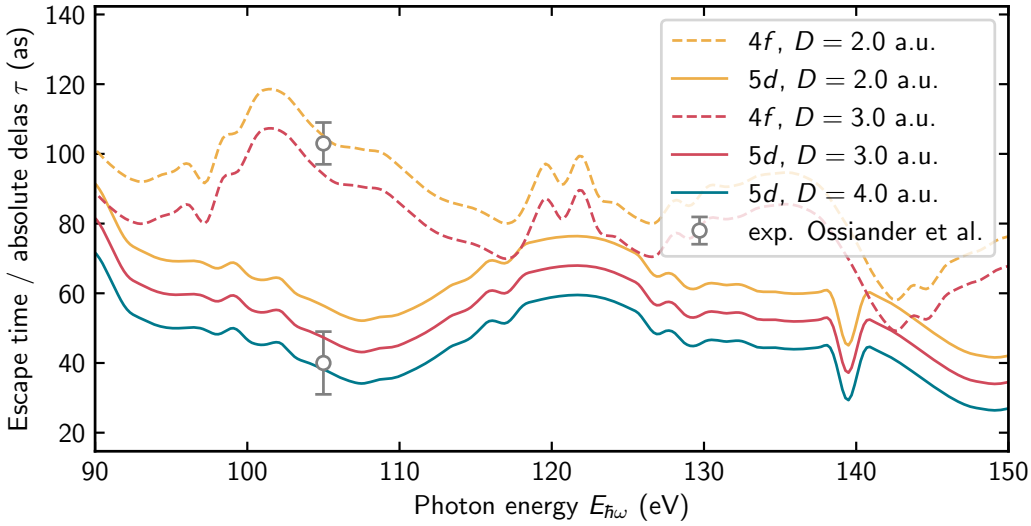

Extended Data Figure 9: Extrapolation of the reference plane's position. Best simulatneous agreement for the VB and W4f states with the experiment in [10] is reached for $D = 3$ a.u. i.e. approx 70% of the W(110) lattice spacing.

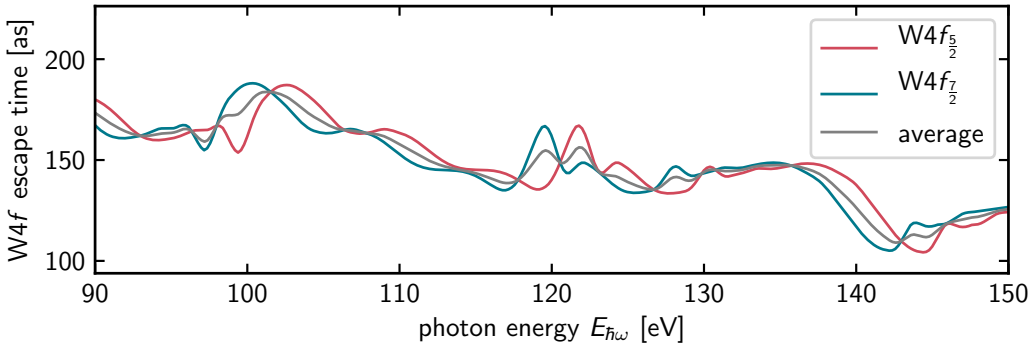

Extended Data Figure 10: Escape times of the unresolved spin-orbit split components of the W4f photoemission. We don't find any significant differences beyond their shift in energy.

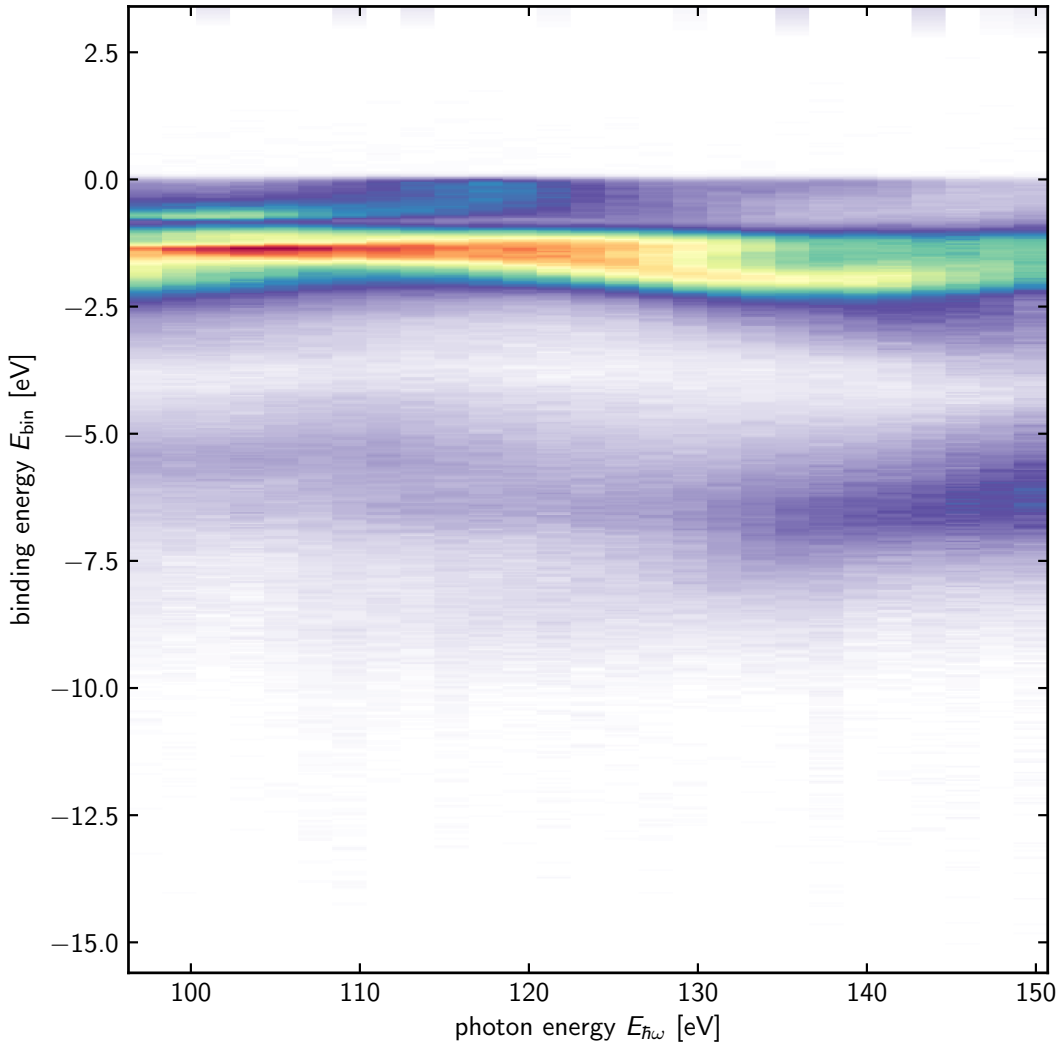

Extended Data Figure 11: High resolution photoemission spectrogram of the W(110) valence band between 96 eV and 145 eV. The dominant 5*d* band with its characteristic spoon-like feature at ~ 140 eV is found above 3 eV binding energy. The lower lying *sp*-band does not significantly contribute to the photoelectron signal in the attosecond experiment wherefore we are not sensitive to it.